

## PAPER

[View Article Online](#)  
[View Journal](#) | [View Issue](#)Cite this: *J. Mater. Chem. A*, 2024, **12**, 5760

## Cobalt-based current collectors for flexible electrodes and their application in lithium–sulfur batteries†

Ying Yu,<sup>a</sup> Zhenkai Tang,<sup>a</sup> Yuxiao Wang,<sup>bc</sup> Hongzhang Zhang,<sup>b</sup> Huamin Zhang<sup>b</sup> and Xianfeng Li<sup>b</sup>

Flexible energy storage devices with high energy density and excellent mechanical properties have attracted great interest in the development of flexible electrodes. However, flexible electrodes don't have current collectors, limiting their battery performance. To improve the performance of flexible electrodes, a cobalt-based (Co-based) current collector was designed and fabricated. It is proved that the Co-based current collector is promising due to high conductivity, light weight, continuity and close contact with the electrode. Meanwhile, when the Co-based current collector is applied in lithium–sulfur batteries, it can physically and chemically restrict polysulfides and inhibit the shuttle effect. As a result, Li–S batteries assembled with Co modified electrodes deliver a specific discharge capacity of 899 mA h g<sup>−1</sup> at 1C. And a high reversible capacity of 639 mA h g<sup>−1</sup> and capacity retention of 56.1% can also be achieved at 0.1C even after continuously running for 200 cycles with a high sulfur loading of 8 mg cm<sup>−2</sup>.

Received 13th November 2023

Accepted 25th January 2024

DOI: 10.1039/d3ta06966d

[rsc.li/materials-a](https://rsc.li/materials-a)

## Introduction

Due to the increasing demand for multifunctional electronic devices to be lighter, thinner, and smaller, flexible electronic devices have become one of the most intensive research hot-spots.<sup>1,2</sup> Flexible electrodes, as the key to flexible electronic devices, have been extensively studied in different materials and manufacturing technologies.<sup>3,4</sup> Flexible electrodes are explored for high energy density batteries since they can achieve high active material loading and rapid Li<sup>+</sup> transmission as well as avoid heavy metal current collectors.<sup>5,6</sup> For example, a mesoporous hierarchical NiCoSe<sub>2</sub>–NiO composite self-supported on a carbon nanoarray electrode achieves a cycle capacity of 919.43 mA h g<sup>−1</sup> at 0.2C with a high sulfur loading (3.5 mg cm<sup>−2</sup>).<sup>7</sup> In addition, 3D porous frameworks,<sup>8</sup> doping polar materials<sup>9</sup> and doping polar groups<sup>10</sup> can enhance the electron/ion conductivity between the flexible electrode's interior and interface; doping SO<sub>4</sub><sup>2−</sup> anions in a 3D PPy–SO<sub>4</sub> inter-connected framework skeleton enhanced the conductivity of PPy to accelerate the electrode reaction.<sup>11</sup> However, due to the lack of current collectors, the electronic conduction in the electrode

can only rely on the conductive skeleton of the electrode. The electronic conduction between the flexible electrodes and plate or shell of batteries is limited by point-to-point conduction, which limits battery performance. In addition, it is too hard to weld the tabs on the flexible electrodes without current collectors. As a result, it is difficult for a further scale-up process in practice, such as assembling soft pack batteries. Therefore, how to configure current collectors for flexible electrodes has become a challenging topic.

Metal foil current collectors with excellent electron conductivity have been widely used in traditional energy storage devices, *e.g.* aluminum (Al) foil and copper (Cu) foil. However, a metal foil current collector is easily separated from the electrode material when the electrode is bent or the active material loading of the electrodes is high. Meanwhile, the high area mass of metal foil will also reduce the energy density of batteries. It is an excellent solution to modify the surface by using metal foil *via* reactive-ion etching or other processes.<sup>12</sup> For example, a thin copper layer current collector (<1 μm) made by RF-magnetron sputtering provides flexibility to the electrode and has highlighted the performance of Si anodes.<sup>13</sup> An ultrathin Ni–P layer made by the quasi-stable electroless deposition method is proposed to fabricate flexible electrodes with satisfactory electrochemical performance and flexibility.<sup>14</sup> However, the research on current collectors is not yet satisfactory. Typically, conductivity of current collectors and complexity of the production process still hinder their practical application.

Herein, a Co-based thin layer was prepared to modify the flexible porous electrode *via* electroless deposition, which is a mature industrial application technology due to its simple

<sup>a</sup>College of Chemical Engineering, State Key Laboratory of Materials-Oriented Chemical Engineering, National Engineering Research Center for Special Separation Membrane, Nanjing Tech University, Nanjing, 211816, China. E-mail: yuying2020@njtech.edu.cn

<sup>b</sup>Department Division of Energy Storage, Dalian Institute of Chemical Physics, Chinese Academy of Sciences, Zhongshan Road 457, Dalian 116023, China

<sup>c</sup>University of Chinese Academy of Sciences, Beijing 100049, China

† Electronic supplementary information (ESI) available. See DOI: [10.1039/d3ta06966d](https://doi.org/10.1039/d3ta06966d)

process equipment, uniform coating and high substrate selectivity. The Co-based layer has good stability and high conductivity. It's also continuous and closely in contact with the porous electrode; thus it can work as a current collector to enhance the electronic conduction of the electrode. In addition, it is reported that cobalt compounds can fix polysulfides and catalyze the electrochemical reaction of Li-S batteries.<sup>15–17</sup> As a result, lithium-sulfur (Li-S) batteries with high theoretical specific capacity ( $1672 \text{ mA h g}^{-1}$ ) and energy density ( $2600 \text{ Wh kg}^{-1}$ ) are selected as an example to test the cobalt-based current collector performance.<sup>18–21</sup> Based on the characterization and analysis of the Co-based layer structure and physical properties, the working mechanism and application feasibility in Li-S batteries with high sulfur loading are deeply investigated.

## Experimental

### Preparation of the S/C composite

The synthesis procedure of the S/C composite was reported<sup>22</sup> and summarized as follows. 10 g KB nanoparticles were heated to  $900^\circ\text{C}$  at  $5^\circ\text{C min}^{-1}$  under an argon atmosphere in a furnace. Then a flux of steam ( $600 \text{ ml min}^{-1}$ ) was introduced for 90 minutes. Thereafter the furnace was cooled down to room temperature. After mixing the obtained product and sulfur in a weight ratio of 1 : 3, the mixture was ball-milled for 6 h and then heated at  $155^\circ\text{C}$  for 15 h in an argon filled vessel. Finally, the S/C composite with 75 wt% S was obtained.

### Preparation of electrodes

The flexible electrodes were obtained by phase inversion as in our previous work.<sup>23</sup> In short, a homogeneous slurry was cast onto a clean and flat glass plate. Next, the glass plate coated with the slurry was immersed in a water coagulation bath, and then the wet electrode was peeled off spontaneously. The wet electrode was washed with deionized water and then freeze-dried at low temperature ( $<-40^\circ\text{C}$ ) and pressure ( $<10 \text{ Pa}$ ). The freeze-dried electrodes were used as a control and labeled as PE (porous electrodes). The sulfur loading of electrodes is controlled by the thickness of the blade-coating slurry.

For electrodes with  $2.5 \text{ mg cm}^{-2}$  sulfur loading, the homogeneous slurry was prepared by mixing 80 wt% S/C composite and 20 wt% polyvinylidene fluoride-hexafluoro propylene (PVDF-HFP) in 1-methyl-2-pyrrolidinone (NMP). The solid content is 11.4 wt%.

For electrodes with  $8 \text{ mg cm}^{-2}$  sulfur loading, the homogeneous slurry was prepared by mixing 65 wt% S/C composite, 10 wt% Super P and 25 wt% polyvinylidene fluoride-hexafluoro propylene (PVDF-HFP) in 1-methyl-2-pyrrolidinone (NMP). The solid content is 17.4 wt%.

The cobalt-based current collector modified flexible porous electrode was prepared by electroless deposition. The PE and nickel foam were made to come into close contact and then fixed on the glass plate to prevent being damaged during the electroless deposition process. Next, the electrode with nickel foam and the glass plate was placed in an electroless bath and heated in an  $85^\circ\text{C}$  water bath for 4 h. The schematic diagram of

electroless deposition is shown in Fig. S1.† The electroless bath consisted of cobalt sulfate ( $\text{CoSO}_4 \cdot 7\text{H}_2\text{O}$ ,  $24 \text{ g L}^{-1}$ ), sodium hypophosphite ( $\text{NaH}_2\text{PO}_2$ ,  $28.8 \text{ g L}^{-1}$ ), ammonium sulfate ( $(\text{NH}_4)_2\text{SO}_4$ ,  $14.4 \text{ g L}^{-1}$ ), and sodium citrate ( $\text{Na}_3\text{C}_6\text{H}_5\text{O}_7 \cdot 2\text{H}_2\text{O}$ ,  $14.4 \text{ g L}^{-1}$ ). The pH of the electroless bath was adjusted to 8.8 by using ammonia solution ( $\text{NH}_3 \cdot \text{H}_2\text{O}$ ). The electrode after electroless deposition was washed with deionized water and then dried in an oven at  $60^\circ\text{C}$  and marked as PE-Co.

### Materials characterization

Microstructural analysis of the samples was conducted by scanning electron microscopy (SEM, JSM-7800F). The electrodes were vacuum dried at 152 K for 24 h before being subsequently transferred to a Micromeritics ASAP 2460 for  $\text{N}_2$  adsorption measurements performed at 77 K. The BET specific surface area and the volume of the cathode pores were estimated based on the obtained isotherms. Three-dimensional imaging was performed by X-ray tomography (XRT, Versa XRM-500). The acceleration voltage of the X-ray tube is 80 kV, the sample stage rotates  $360^\circ$ , two-dimensional projections are collected at equal angular intervals, and then three-dimensional reconstruction is performed. The exposure time for each projection is 10 s. The pixel size of the reconstructed image is  $0.6791 \mu\text{m}$ . The atomic force microscope (AFM) images were acquired by using a PARK XE-100. The surface species and their chemical states were analyzed by X-ray photoelectron spectroscopy (XPS, ESCA-LAB250xi, Thermo Fisher). X-ray diffraction (XRD, DX-2700) operated at 40 kV and 30 mA with Cu-K $\alpha$  radiation ( $\lambda = 0.154 \text{ nm}$ ) was used for crystal structure analysis and the XRD data were collected in the  $2\theta$  range from  $10^\circ$  to  $90^\circ$  at a scanning rate of  $1^\circ \text{ min}^{-1}$ . The sulfur content of electrodes was determined by using thermogravimetric analysis (TGA, Pyris-Elmer), in which the temperature was increased from 50 to  $500^\circ\text{C}$  with a heating rate of  $5^\circ\text{C min}^{-1}$  under a  $\text{N}_2$  atmosphere. The electrode resistivity was tested by using a double electric test four-probe tester (RTS-9). An HP-504 probe with an average probe distance of 1.59 mm was used.

### Electrochemical measurements

The electrochemical performance of the Li-S cells was tested with CR2016 coin cells, which were constructed in an Ar-filled glove box. Lithium foil (diameter: 16 mm and thickness: 700  $\mu\text{m}$ ) acted as the anode. The cathode and anode were separated by Celgard 2325 membranes. The electrolyte is 1 M bis(tri-fluoromethylsulfonyl) imide (LiTFSI) in 1,2-dimethoxymethane (DME)/1,3-dioxolane (DOL) (1 : 1, v/v) with 5 wt%  $\text{LiNO}_3$  additive. The electrolyte amounts added in the cell with  $2.5 \text{ mg cm}^{-2}$  and  $8 \text{ mg cm}^{-2}$  sulfur loading are 60  $\mu\text{L}$  and 120  $\mu\text{L}$ , corresponding to electrolyte-to-sulfur ratios of 31 and 19  $\mu\text{L mg}^{-1}$ , respectively. The cathodes were cut into pieces with a diameter of 10 mm. The charge/discharge test was carried out using a LAND CT-2001A system with voltages ranging from 1.75 V to 2.8 V for Li-S cells in a constant temperature box ( $25^\circ\text{C}$ ). The specific capacities mentioned in this article were calculated based on active materials ( $1\text{C} = 1672 \text{ mA g}^{-1}$ ). The voltage mentioned in this article was with respect to  $\text{Li}^+/\text{Li}$  (vs.  $\text{Li}^+/\text{Li}$ ).

The electrochemical impedance spectroscopy (EIS) measurement was conducted under open-circuit conditions in the frequency range from  $3.0 \times 10^6$  Hz to  $1.0 \times 10^{-2}$  Hz with an amplitude of 10 mV on a Solartron 1287 electrochemical workstation. The cyclic voltammetry (CV) curves were obtained for 6 cycles at a scanning rate of  $0.1 \text{ mV s}^{-1}$  in the range of 1.75–2.8 V *via* a CHI 604E. CV curves of symmetric cells were obtained at a scan rate of  $0.5 \text{ mV s}^{-1}$  (potential window  $-1.0$ – $1.0$  V) *via* a CHI 604E.

## Results and discussion

A Co-based current collector was prepared for improving electrochemical performance of flexible electrodes *via* electroless deposition.<sup>24,25</sup> As shown in Scheme 1 and Fig. S1†, a layer of cobalt composite is in ocher and deposited on the surface of the flexible porous electrode (named PE) after the simple electroless deposition process (Fig. S2†). Meanwhile, the electrodes still maintain their flexibility (Fig. S1, Video S1 and S2†) after electroless deposition. The PE XRD peaks (Fig. S3†) are consistent with those of the sulfur and binder in raw materials. The XRD pattern of PE after electroless deposition (labeled as PE-Co) is similar to that of PE; only the peak intensity of each peak is significantly weakened due to the presence of the coating layer. In addition, no new peaks are observed in the PE-Co XRD spectrum, indicating that the Co-based coating layer is amorphous.

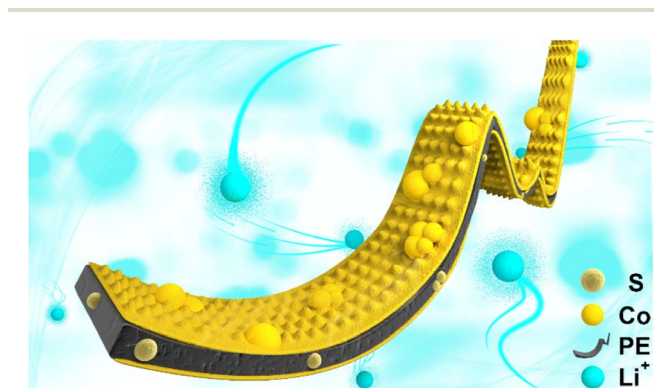
The microtopography of PE and PE-Co is shown in Fig. 1a–h to observe the morphology and location of the electroless deposition layer more clearly. The PE is porous with a fine pore structure on the surface, which can facilitate ion transport. After electroless deposition, PE-Co still maintains a porous structure guaranteeing ion transmission (Fig. 1c), which is also confirmed by the Brunauer–Emmett–Teller (BET) method (Fig. S4 and Table S1†), while the surface of PE-Co is much different from that of PE. There are no pores but some spherical particles on the PE-Co surface. Co-based particles are divided into two types with a particle size of several micrometers (Fig. 1e) and several nanometers (Fig. 1f), which is also proved by atomic force microscopy (AFM, Fig. 1g and h). Furthermore, from the element distribution in the electrode cross section

(Fig. 1i, j and S5†), the elements C, O, S and F are uniformly distributed, which means the raw materials are evenly distributed in the electrode. The element Co is mainly distributed on the upper and lower surfaces of the electrode, indicating that the Co-based coating layer is mainly distributed on the surfaces of the electrode as designed. This is also proven by high-resolution X-ray tomography (XRT, Fig. 1k and l).<sup>26,27</sup> Obviously, the Co-based coating layer is continuous and mainly deposited on the both surfaces of the electrode. Fig. 1l clearly shows the Co-based particle distribution in the electrode. On the one hand, it can provide a continuous conduction path for electrons and improve the current collection effect. On the other hand, a continuous coating layer can physically inhibit polysulfide dissolution out of the cathode and improve cycle performance when applied in Li–S batteries.

Affected by the catalysis of nickel foam, many more Co-based particles are deposited the upper surface of PE-Co (close to the nickel foam side) than on the lower surface (close to the glass plate side). Moreover, because the electroless plating solution can enter the large open holes inside PE, there is a small amount of deposition in the large exposed holes of PE-Co.

The four-probe technique was used to analyze the resistivity of the Co-based coating layer as a current collector. As listed in Fig. 2a, the resistivity of the PE-Co surface is only  $13.9 \text{ } \Omega \text{ cm}^{-1}$ , which is about half that of PE ( $28.3 \text{ } \Omega \text{ cm}^{-1}$ ). The Co-based coating layer significantly improves the conductivity of the electrode surface, and can be an excellent current collector and further increase the utilization of the active material. In addition, the areal density of the current collector also has a great impact on the energy density of batteries. The mass load of the Co-based coating layer in PE-Co is estimated in accordance with the sulfur content of PE and PE-Co. It can be calculated that the sulfur content of PE and high-load PE is 60.0 and 48.8 wt%, respectively, based on the mass ratio during the preparation. According to thermogravimetry analysis (TGA, Fig. 2b), the sulfur content of PE-Co and high-load PE-Co is 52.2 and 47.3 wt%, respectively. The mass loading of sulfur of PE-Co and high-load PE-Co is 2.5 and  $8.0 \text{ mg cm}^{-2}$ , respectively. As a result, it can be calculated that the Co composite content of PE-Co is 13.0 wt%, while the Co composite content of high-load PE-Co is only 3.0 wt%. The corresponding Co composite loadings are about 0.6 and  $0.5 \text{ mg cm}^{-2}$ , respectively. The areal density of pieces of carbon-coated Al foil is about  $3\text{--}5 \text{ mg cm}^{-2}$ , which are commonly used current collectors of cathodes in Li–S batteries. Co-based current collectors with light weight can improve the energy density of Li–S batteries. Therefore, the Co-based current collector prepared by the electroless deposition process is excellent due to its outstanding current collection effect and light weight.

To explore the impact of the Co-based current collector in Li–S batteries, X-ray photoelectron spectroscopy (XPS) of PE-Co and PE-Co after cycling was analyzed. As shown in Fig. 2c, there are some peaks corresponding to the S element for PE-Co. The cobalt-based coating does not completely cover the internal PE, causing some of the sulfur element to be exposed. So the XPS spectrum of PE-Co shows the characteristic peaks of S–S at 162.1 and  $163.5 \text{ eV}$ .<sup>28,29</sup> Meanwhile, XPS of PE-Co has



**Scheme 1** The structure of the electrode modified by using the Co-based current collector (PE-Co).





Fig. 1 (a) Cross-section and (b) surface morphology of PE. (c) Cross-section and (d–f) surface morphology of PE-Co at different magnifications. (g and h) AFM phase images of the surface of PE-Co. (i) Cross-section morphology of PE-Co and (j) elemental mapping of Co. (k) 2D and (l) 3D distribution of the cobalt-based coating in PE-Co acquired by X-ray tomography (XRT).

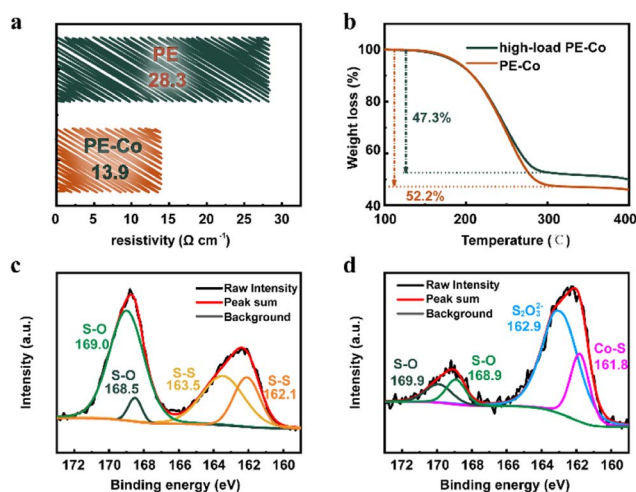


Fig. 2 (a) The resistivity of PE and PE-Co. (b) TGA curves of PE-Co and PE-Co with high sulfur loading. XPS spectra for S of (c) PE-Co and (d) PE-Co after cycling.

characteristic peaks belonging to sulfate or sulfite at 168.5 and 169.0 eV, which are residual or generated during the electroless deposition.<sup>30,31</sup> In addition, the XPS spectrum of the cycled PE-Co (Fig. 2d) shows a new peak at 161.8 eV.<sup>32</sup> This is the characteristic peak of the Co-S bond, indicating that there is a chemical interaction between the Co-based current collector and polysulfide. As a result, the Co-based current collector can fix polysulfide within the cathode *via* the Co-S bond, thereby

improving the cycle performance and life of batteries. The other peaks in the XPS spectrum of PE-Co after cycling are characteristic peaks of thiosulfate, sulfite and sulfate, which are formed by oxidation of unstable polysulfide ions exposed to air or the residue of sulphate.

In order to evaluate the influence of Co-based current collectors on the electrochemical behavior of batteries, electrochemical performance of batteries assembled with PE-Co and PE was tested. The cyclic voltammetry curves of batteries assembled with PE show two reduction peaks and one oxidation peak similar to those of a typical Li-S battery (Fig. 3a and S6a†).<sup>33</sup> The two reduction peaks correspond to the two-step reduction of sulfur to lithium sulfide ( $\text{Li}_2\text{S}$ ), and one oxidation peak represents the reversible oxidation process of the discharge product to elemental S. However, the cyclic voltammetry curve of batteries assembled with PE-Co is different from that of batteries assembled with PE (Fig. 3a and S6b†). Their oxidation peak splits into two peaks due to the Co-based current collector improving the PE-Co conductivity and reducing battery polarization.<sup>33</sup> Thus, the potential difference between oxidation peaks and reduction peaks in the CV curves of the battery assembled with PE-Co is also significantly smaller than that of PE. Moreover, batteries assembled with PE-Co have larger peak current in the CV curves. In addition, the Tafel slopes of the Li-S batteries assembled with PE-Co and PE derived from the anodic peak and two cathodic peaks are shown in Fig. 3b–d. By fitting the anodic and cathodic peaks, the batteries assembled with PE-Co show lower Tafel slopes,

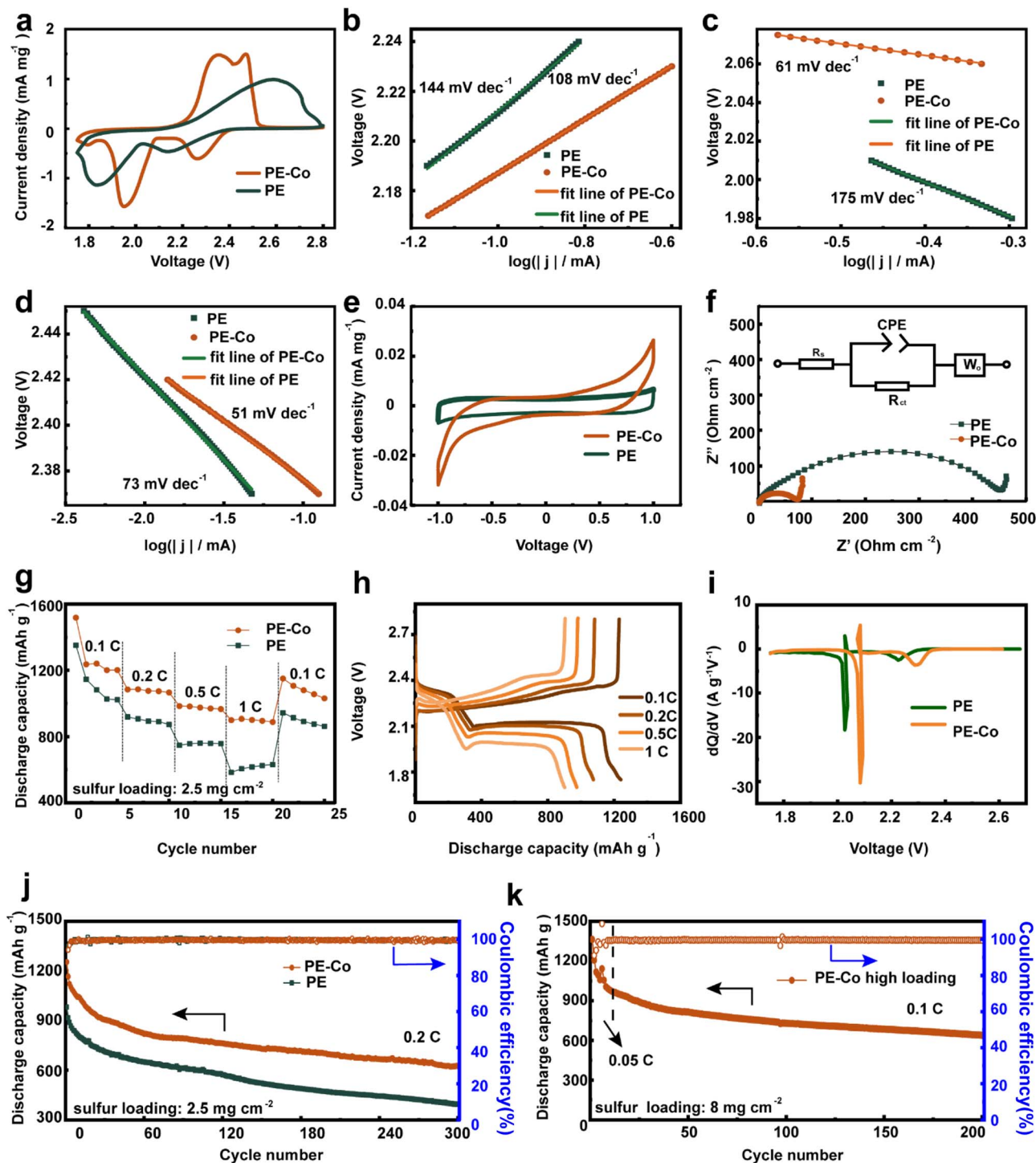


Fig. 3 (a) CV curves of batteries assembled with PE and PE-Co at the 5th cycle. Tafel slopes from the anodic peak (b) and cathodic peaks (c and d) of the CV curves. (e) CV curves of symmetric cells at 0.5 mV s<sup>-1</sup>. (f) EIS plots of batteries assembled with PE and PE-Co. The inset shows the used equivalent circuit. (g) Rate performance of batteries assembled with PE and PE-Co at various C-rates from 0.1 to 1C. (h) Charge/discharge curves of batteries assembled with PE-Co at various C-rates from 0.1 to 1C. (i) The dQ/dV ~ V curves of batteries assembled with PE and PE-Co discharged at 0.2C. (j) Cycling performance of batteries assembled with PE and PE-Co at 0.2C. (k) Cycling performance of the Li-S batteries assembled with 8 mg cm<sup>-2</sup> sulfur loaded PE-Co at 0.1C.

indicating that the Co based current collector has catalytic activity for the reduction and oxidation of S<sub>8</sub>, LiPSs, and Li<sub>2</sub>S<sub>2</sub>/Li<sub>2</sub>S.<sup>34</sup>

To further demonstrate the effectiveness of Co-based current collectors in catalyzing the conversion of LiPSs, symmetrical cells with Li<sub>2</sub>S<sub>6</sub> were assembled. As shown in Fig. 3e, the current response of PE-Co symmetrical cells is higher than that of the



PE electrode, further confirming the catalytic activity. Fig. 3f shows the electrochemical impedance (EIS) test results of batteries assembled with PE and PE-Co. The electrochemical impedance spectra are composed of a semicircle and a diagonal line, which represents the charge transfer resistance ( $R_{ct}$ ) at the electrode/electrolyte interface and the Warburg impedance ( $W_0$ ). According to the equivalent circuit fitting shown in Fig. 3f, the  $R_{ct}$  of batteries assembled with PE-Co is only  $65.2 \Omega \text{ cm}^{-2}$ , while the  $R_{ct}$  of batteries assembled with PE is  $421.1 \Omega \text{ cm}^{-2}$ , which is almost 6.5 times that of batteries assembled with PE-Co. This is because the Co-based current collector improves the electrode conductivity and reduces charge transfer resistance. Meanwhile, the diffusion coefficient of  $\text{Li}^+$  ( $D$ ) of PE-Co ( $4.74 \times 10^{-10} \text{ cm}^2 \text{ s}^{-1}$ ) is found to be 4.3 times that of PE ( $1.09 \times 10^{-10} \text{ cm}^2 \text{ s}^{-1}$ ) via quantitatively analyzing the relationships between  $Z'$  and  $\omega^{-1/2}$  in the low frequency region (Fig. S7 and Table S2†).<sup>33</sup> So the better rate and cycle performance of batteries with PE-Co can be expected.

The rate performance of batteries assembled with PE and PE-Co was tested from 0.1C to 1C (Fig. 3g and h). The specific discharge capacity at 0.1, 0.2, 0.5 and 1C of Li-S batteries assembled with PE-Co are 1280, 1077, 975 and  $899 \text{ mA h g}^{-1}$ , respectively. When the rate returns to 0.1C, the specific discharge capacity recovers to  $1084 \text{ mA h g}^{-1}$ . While the batteries assembled with PE show 1125, 897, 757, 612 and  $897 \text{ mA h g}^{-1}$  at 0.1, 0.2, 0.5, 1 and 0.1C (Fig. S8†). Two types of electrodes have similar matrix and internal  $\text{Li}^+$  diffusion paths. Therefore, the only reason for the improvement of battery rate performance is that the continuous Co-based current collector PE-Co improves the conductivity of the electrode and suppressed the dissolution of polysulfides.

It is well known that it is difficult for sulfur to fully participate in the reaction due to its poor conductivity during the first discharge process. Meanwhile, soluble intermediate product generating during the reaction and diffusing into the electrolyte can lead to the loss of active materials. Therefore, the capacity of first discharge is always less than the theoretical specific capacity ( $1672 \text{ mA h g}^{-1}$ ). The first discharge specific capacity of the battery assembled with PE-Co is up to  $1253 \text{ mA h g}^{-1}$  at 0.2C, which is significantly higher than that of PE ( $983 \text{ mA h g}^{-1}$ , Fig. 3j). The huge difference in the first discharge specific capacity is due to the influence of the Co-based current collector on the electrode surface. The Co-based current collector improves the electronic conduction of the flexible electrode and hinders the diffusion of polysulfides by providing physical barriers and chemical force. As a result, it increases the utilization of sulfur and the specific capacity of the first discharge. In the subsequent cycle, the continuous Co-based current collector still plays a role and improves the cycle performance of batteries. Moreover, the  $dQ/dV \sim V$  curves of batteries discharged at 0.2C can further illustrate the advantages of the Co-based based current collector. As shown in Fig. 3j, reversible capacity remains at  $624 \text{ mA h g}^{-1}$ , corresponding to a high capacity retention of 55.6% (calculated based on the 3rd discharge specific capacity) for batteries with PE-Co after 300 cycles, which is much better than that of PE (discharge specific capacity at the 300th cycle:  $396 \text{ mA h g}^{-1}$  and capacity retention:

44.5%). The cycle stability and discharge capacity have also been improved at a current density of  $1.2 \text{ mA}$  (Fig. S9†). In addition, the sulfur fixation effect of the Co-based current collector is also further proved by the visual experiment (Fig. S10†).

To further investigate the practicality of Co-based current collectors, cathodes with high sulfur loading were prepared with the same method. The electrochemical performance is shown in Fig. 3k. Batteries with  $8 \text{ mg cm}^{-2}$  sulfur loaded PE-Co display  $1363 \text{ mA h g}^{-1}$  at 0.05C in the initial discharge and  $1140 \text{ mA h g}^{-1}$  at 0.1C after activation, indicating that the Co-based collector improves the electronic conductivity of electrodes. An excellent capacity of  $639 \text{ mA h g}^{-1}$  and capacity retention of 56.1% could still be obtained after 200 cycles. This is obviously because the Co-based current collector can also fix polysulfide and inhibit polysulfide shuttling. As shown in Table S3,† compared with high load flexible batteries, the battery performance has advantages over assembled non-carbon 3D skeleton electrodes, which are slightly inferior in conductivity to carbon 3D skeleton electrodes (such as graphene, carbon cloth, etc.), especially porous electrodes made by phase inversion. This also indicates that cobalt based current collectors are suitable for non-carbon 3D skeleton electrodes and can further expand their development advantages.

In order to study whether the Co-based current collector can adapt to the charge and discharge process or not, the morphology of PE and PE-Co after cycling was observed. As shown in Fig. 4 and S11,† both PE and PE-Co after cycling show similar morphology to that of electrodes before cycling. Additionally, the Co-based current collector still retains close contact with the porous electrode during cycling, and the metal Co particles have no noticeable cracks or defects. As for the perspective of element distribution, the distribution of C, O and



Fig. 4 (a) Surface and (b and c) cross-section morphology of PE-Co after cycling and elemental mapping of (d) C, (e) O, (f) Co, (g) S and (h) F.

F elements has not changed, and they are still evenly distributed in the electrode. The S element distribution has nothing to do with the electrode structure, and it is evenly distributed in the entire electrode space, which is mainly because sulfur dissolves and redeposits during the charge and discharge reaction. The element Co is still mainly distributed on the electrode surfaces. The Co-based current collector can still maintain its original shape and adapt to the volume change during the charging and discharging process. It can always play roles of “current collection” and “inhibiting polysulfide shuttling” during the charging and discharging process.

## Conclusions

In summary, a cobalt-based current collector was designed and prepared *via* a simple electroless deposition method. It is a wonderful current collector for flexible electrodes because it is not only lighter than commonly used metal foil current collectors (Al or Cu foil), but also has high conductivity due to its continuity and close contact with the electrode. When applied in Li-S batteries, Co-based current collectors can also strongly immobilize polysulfides through physical barriers and chemical bonding. Benefiting from the Co-based current collectors, a high S utilization of 899 mA h g<sup>-1</sup> can be realized at 1C. A high reversible capacity of 624 mA h g<sup>-1</sup> and capacity retention of 55.6% can also be achieved at 0.2C after 300 cycles for batteries assembled with Co-based current collector modified electrodes. Even when the sulfur loading increases to 8 mg cm<sup>-2</sup>, the batteries still show a high specific capacity of 1140 mA h g<sup>-1</sup> at 0.1C. Based on our results with a thin Co-film as a current collector, the battery performance has been improved, which highlights the application for flexible electrodes.

## Author contributions

Ying Yu: investigation, formal analysis, writing – original draft preparation, conceptualization. Zhenkai Tang: investigation, visualization, data curation. Yuxiao Wang: formal analysis, writing – reviewing and editing. Hongzhang Zhang: conceptualization, writing – reviewing and editing, funding acquisition. Huamin Zhang: supervision, project administration, funding acquisition. Xianfeng Li: supervision, project administration, funding acquisition.

## Conflicts of interest

There are no conflicts to declare.

## Acknowledgements

The authors acknowledge the financial support from the National Natural Science Foundation of China (No. 22308152, 51673199, 51972301, and 51677176), National Key Research and Development Program of China (2021YFB3801301), Youth Innovation Promotion Association of CAS (2015148), Youth Innovation Foundation of DICP (ZZBS201615 and ZZBS201708), Dalian Outstanding Young Scientific Talent (2018RJ03),

National Key Research and Development Project (2019YFA0705600) and Priority Academic Program Education Institutions (PAPD). The authors also express appreciation to Shaogang Wang from the Shenyang National Laboratory for Materials Science, Institute of Metal Research, Chinese Academy of Sciences, for his help in electrode structure analysis by X-ray diffraction topography (XRT).

## Notes and references

- 1 C. Wang, X. Zeng, P. J. Cullen and Z. Pei, *J. Mater. Chem. A*, 2021, **9**, 19054–19082.
- 2 Y. He, B. Matthews, J. Wang, L. Song, X. Wang and G. Wu, *J. Mater. Chem. A*, 2018, **6**, 735–753.
- 3 Y. Wang, Q. Yang, Y. Zhao, S. Du and C. Zhi, *Adv. Mater. Technol.*, 2019, **4**, 1900083.
- 4 Y. Li, R. Wang, Z. Guo, Z. Xiao, H. Wang, X. Luo and H. Zhang, *J. Mater. Chem. A*, 2019, **7**, 25227–25246.
- 5 A. Eftekhari and D.-W. Kim, *J. Mater. Chem. A*, 2017, **5**, 17734–17776.
- 6 H. Pan, Z. Cheng, J. Chen, R. Wang and X. Li, *Energy Storage Mater.*, 2020, **27**, 435–442.
- 7 T. Li, K. Liu, S. Wang, Z. Liu, G. Liao, Z. Chen and P. Shen, *J. Colloid Interface Sci.*, 2023, **629**, 114–124.
- 8 Y.-W. Tian, Y. Yu, L. Wu, M. Yan, W.-D. Dong, C.-Y. Wang, H. S. H. Mohamed, Z. Deng, L.-H. Chen, T. Hasan, Y. Li and B.-L. Su, *J. Energy Chem.*, 2023, **85**, 1–10.
- 9 Y. W. Tian, Y. J. Zhang, L. Wu, W. D. Dong, R. Huang, P. Y. Dong, M. Yan, J. Liu, H. S. H. Mohamed, L. H. Chen, Y. Li and B. L. Su, *ACS Appl. Mater. Interfaces*, 2023, **15**, 6877–6887.
- 10 G. Yu, G. Ye, C. Wang, C. Wang, Z. Wang, P. Hu, Y. Li, X.-X. Feng, S.-J. Tan, M. Yan, S. Xin and Z. Liu, *Sci. China: Chem.*, 2023, **67**, 247–259.
- 11 G. Yu, C.-Y. Wang, W. Dong, Y.-W. Tian, Z. Wang, J. Lu, P. Hu, Y. Liu, M. Yan, Y. Li and Z. Liu, *J. Colloid Interface Sci.*, 2024, **654**, 201–211.
- 12 M.-H. Park, M. Noh, S. Lee, M. Ko, S. Chae, S. Sim, S. Choi, H. Kim, H. Nam and S. Park, *Nano Lett.*, 2014, **14**, 4083–4089.
- 13 J. Y. Choi, D. J. Lee, Y. M. Lee, Y. G. Lee, K. M. Kim, J. K. Park and K. Y. Cho, *Adv. Funct. Mater.*, 2013, **23**, 2108–2114.
- 14 J. Gou, H. Zhang, X. Yang, Y. Chen, Y. Yu, X. Li and H. Zhang, *Adv. Funct. Mater.*, 2018, **28**, 1707272.
- 15 J. Li, W. Xie, S. Zhang, S. Xu and M. Shao, *J. Mater. Chem. A*, 2021, **9**, 11151–11159.
- 16 Z. Sun, S. Vijay, H. H. Heenen, A. Y. S. Eng, W. Tu, Y. Zhao, S. W. Koh, P. Gao, Z. W. Seh, K. Chan and H. Li, *Adv. Energy Mater.*, 2020, **10**, 1904010.
- 17 W. Ren, W. Ma, M. M. Umair, S. Zhang and B. Tang, *ChemSusChem*, 2018, **11**, 2695–2702.
- 18 Y. Yang, W. Xu, R. Guo, L. Liu, S. Wang, D. Xie and Y. Wan, *J. Power Sources*, 2014, **269**, 15–23.
- 19 Y. Song, W. Cai, L. Kong, J. Cai, Q. Zhang and J. Sun, *Adv. Energy Mater.*, 2019, 1901075.
- 20 A. Bhargav, J. He, A. Gupta and A. Manthiram, *Joule*, 2020, **4**, 285–291.

- 21 Y. Cao, Y. Lin, J. Wu, X. Huang, Z. Pei, J. Zhou and G. Wang, *ChemSusChem*, 2020, **13**, 1392–1408.
- 22 M. Wang, H. Zhang, Q. Wang, C. Qu, X. Li and H. Zhang, *ACS Appl. Mater. Interfaces*, 2015, **7**, 3590–3599.
- 23 X. Yang, Y. Chen, M. Wang, H. Zhang, X. Li and H. Zhang, *Adv. Funct. Mater.*, 2016, **26**, 8427–8434.
- 24 Y. H. Zhu, S. Yuan, D. Bao, Y. B. Yin, H. X. Zhong, X. B. Zhang, J. M. Yan and Q. Jiang, *Adv. Mater.*, 2017, **29**, 1603719.
- 25 E. Ergul, H. I. Kurt, M. Oduncuoglu and N. F. Yilmaz, *Mater. Res. Express*, 2020, **7**, 115604.
- 26 L. Zhang and S. Wang, *Materials*, 2018, **11**, 1795.
- 27 S. Wang and L. Zhang, *Acta Metall. Sin.*, 2013, **49**, 897–910.
- 28 X.-R. Yu, F. Liu, Z.-Y. Wang and Y. Chen, *J. Electron Spectrosc. Relat. Phenom.*, 1990, **50**, 159–166.
- 29 H. Peisert, T. Chassé, P. Streubel, A. Meisel and R. Szargan, *J. Electron Spectrosc. Relat. Phenom.*, 1994, **68**, 321–328.
- 30 Y. Yang, G. Yu, J. J. Cha, H. Wu, M. Vosgueritchian, Y. Yao, Z. Bao and Y. Cui, *ACS Nano*, 2011, **5**, 9187–9193.
- 31 Q. Qu, T. Gao, H. Zheng, Y. Wang, X. Li, X. Li, J. Chen, Y. Han, J. Shao and H. Zheng, *Adv. Mater. Interfaces*, 2015, **2**, 1500048.
- 32 G. Stevens and T. Edmonds, *J. Less-Common Met.*, 1977, **54**, 321–330.
- 33 Y. Yu, H. Zhang, X. Yang, J. Gou, X. Tong, X. Li and H. Zhang, *Energy Storage Mater.*, 2019, **19**, 88–93.
- 34 C. Zhou, M. Chen, C. Dong, H. Wang, C. Shen, X. Wu, Q. An, G. Chang, X. Xu and L. Mai, *Nano Energy*, 2022, **98**, 107332.